Journal of Electronic Materials (2022) 51:2709–2715
https://doi.org/10.1007/s11664-022-09566-y

TOPICAL COLLECTION: SYNTHESIS AND ADVANCED CHARACTERIZATION OF MAGNETIC OXIDES

Wet H_2 Reduction: A Robust Way of Converting α-Fe_2O_3 into Fe_3O_4 at the Nanoscale

Murtaza Bohra[1]

Received: 28 November 2021 / Accepted: 1 March 2022 / Published online: 19 March 2022

Abstract
Iron oxides are a ubiquitous class of magnetic materials, holding the promise of spintronic devices and magnetic hyperthermia based on their tunable magnetic and electric conducting properties. However, their high sensitivity towards oxidation/reduction environments makes them difficult to control in a reversible and scalable manner. Here we demonstrate two different approaches for reduction of antiferromagnetic insulator α-Fe_2O_3 thin films into ferrimagnetic conductor Fe_3O_4 thin films. The wet H_2 reduction process is more efficient than the vacuum and inert gas atmosphere when producing nanocrystalline Fe_3O_4 thin films. We measure low-temperature physical properties and find that the wet H_2 reduction process drives pronounced changes in magnetic anisotropy, Verwey transition, and surface spin canting-induced exchange bias in Fe_3O_4 thin films. We also explain how phase formation in nanocrystalline iron oxide thin films is different from their bulk equilibrium phase diagram.

Keywords Thermal reduction methods · iron-oxide thin films · Verwey transition

Introduction

Earth-abundant iron oxides are exotic materials on account of their unique properties, such as chemical and thermal stability and reduced toxicity over other conventional oxides.[1–6] The rich Fe-O phase diagram consists of many technologically important oxide phases including FeO, α, β, γ, and ζ variants of Fe_2O_3, and Fe_3O_4 promise futuristic nanotronics and nanobiotechnological applications.[5,7,8] On the one hand, antiferromagnetic (FeO and α-Fe_2O_3) oxides can play a key role in emergent antiferromagnetic spintronics, [9] wherein Neel temperatures (T_N) can be tuned by controlling their size and introducing strain in the nanostructures. On the other hand, ferrimagnetic (γ-Fe_2O_3 and Fe_3O_4) oxides not only have been customized for magnetic hyperthermia, [10] but also have potential in homojunction devices such as magnetic tunnel junctions, spin filters, and spin Seebeck effect geometries,[11–14] in which tunable insulating-to-conducting layers are required of the same materials. The magnetic and conducting properties of iron-oxide thin films are strongly dependent on the growth conditions, especially on oxygen partial pressure and growth temperatures,[13,15–17] owing to the sharp phase boundaries among the various iron oxides.[2,13] Consequently, an in-depth study and understanding on formation of iron-oxide thin films across phase boundary and their correlated properties is a demand of our time.

Comprehensive work regarding the growth of iron-oxide thin films using various deposition techniques has been cumulatively performed by many groups,[2,13,14] but the thermodynamic theory of the growth of their nanostructures remains elusive. Although we know that phase formation in iron-oxide structures depends upon growth conditions,[13,15–17] the effect of the post-reduction process on the magnetic properties of iron-oxide thin films have not been explored rigorously. Here, we investigate how these properties can be easily tuned in sputtered iron-oxide thin films depending on the choice, amount, and oxidation state of Fe ions at the nanoscale through specific post-reduction routes used for their fabrication.

✉ Murtaza Bohra
murtazaphy@gmail.com

[1] Mahindra University, École Centrale School of Engineering (MEC), Survey Number 62/1A, Bahadurpally, Jeedimetla, Hyderabad, Telangana 500043, India

Experimental

In the first step, iron-oxide thin films were sputtered from an α-Fe_2O_3 target onto fused quartz substrates at three different radio-frequency (RF) power levels (P): 50, 100, and 200 W in a pure argon gas atmosphere of 7.2×10^{-3} mbar at room temperature. The substrates were neither heated nor cooled during the sputter deposition. In the second step, as-grown (AG) films were subjected to two different reduction processes, namely, vacuum annealing (VA) and wet H_2 annealing (HA) to produce single-phase Fe_3O_4 films. The reduction of α-Fe_2O_3 in the HA and VA process can be described by $3Fe_2O_3+H_2 \rightarrow 2Fe_3O_4+H_2O$ and $3Fe_2O_3 \rightarrow 2Fe_3O_4+1/2O_2$, respectively.[17] For the VA process, the AG films were in situ-annealed at 500 °C for 1 h under dynamic vacuum ~4×10^{-6} mbar. In the HA process, the AG films were ex situ-annealed at 450 °C in H_2/H_2O gas atmosphere for 15 min in a tubular furnace with flow control. X-ray diffraction (XRD) analysis of the films was performed by a PANalytical X'Pert PRO x-ray diffractometer using CuKα radiation. Electrical transport measurements were performed using a four-probe method between 30 and 300 K. The magnetic properties were measured using a Quantum Design Physical Property Measurement System (PPMS). The zero-field cooled magnetization (ZFC) was measured first by cooling the samples from room temperature to 5 K in zero applied field, after which a field of 5 kOe was applied and the magnetization was measured whilst increasing the temperature to 305 K. X-ray photoelectron spectra (XPS) were collected on a Microtech Unit ESCA 3000 Spectrometer with source Mg Kα (1256.6 eV).

Results

XRD patterns of the AG, HA, and VA films at different RF power are given in Fig. 1. The XRD pattern of the AG film does not show any XRD peaks at 50 W, but as we increase the RF power to 100 W, two sharp peaks appear at around 2θ of 35.60° and 63.99°. The former peak (2θ = 35.60°) may be indexed to either the (110) planes of α-Fe_2O_3 or the (311) planes of Fe_3O_4, and the latter peak (2θ = 63.99°) to the (300) planes of α-Fe_2O_3 with some modification of lattice parameters. However, interestingly, in 200 W films, these two peaks shift towards lower 2θ values which are closer to the (311) and (440) planes of Fe_3O_4. The lattice parameters of these films are calculated in Table I by assuming them to be either the hexagonal α-Fe_2O_3 phase or the cubic Fe_3O_4 phase, and indicate that α-Fe_2O_3 is the dominant phase in the 100 W film and Fe_3O_4 in the 200 W film.

In comparison, XRD patterns of HA and VA films do not show any α-Fe_2O_3 phase at any of the RF power used. Three low-intensity XRD peaks (311), (220), and (440) of the Fe_3O_4 phase can be seen in 50 W films, which later increase

Table I Lattice parameters calculated for hexagonal α-Fe_2O_3 and cubic Fe_3O_4 phases for AG films

RF power (W)	*a* (Å) α-Fe_2O_3 (bulk$^{\alpha\text{-}Fe2O3}$: *a* (Å)= 5.038 and *c* (Å) =13.77)	*c* (Å)	*a* (Å) Fe_3O_4 (bulk^{Fe3O4}: *a* (Å)= 8.39)
100	5.037	–	8.28
200	5.069	13.29	8.39

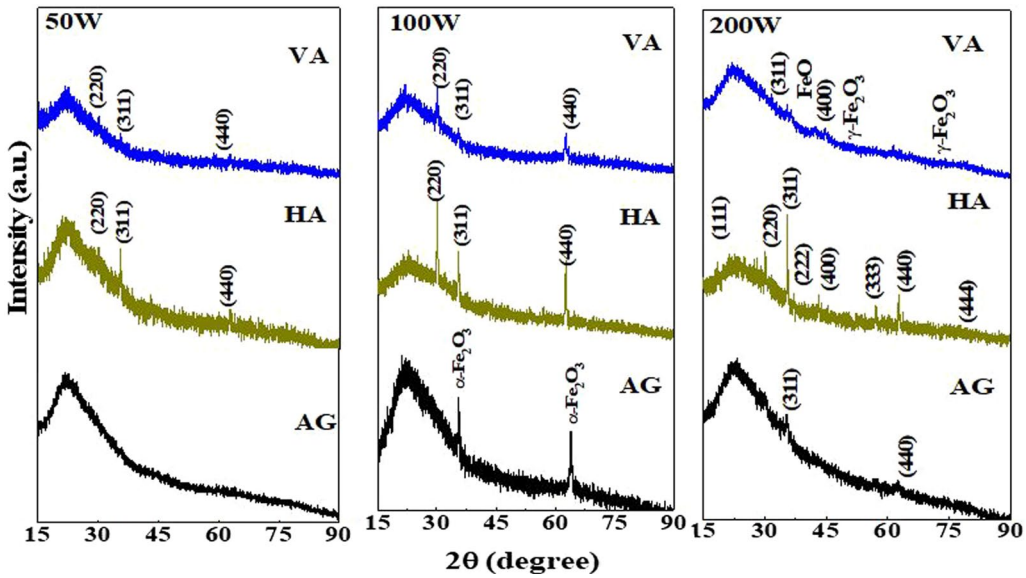

Fig. 1 XRD patterns for AG, HA, and VA films at different RF power.

in intensity in 100 W films, exhibiting (0) texture in both the HA and VA cases. At the higher power of 200 W, the HA films show XRD pattern typical of a randomly oriented Fe_3O_4, while VA films contain impurity FeO and γ-Fe_2O_3 phases along with the Fe_3O_4 phase. The average grain sizes and lattice parameters of Fe_3O_4 phases in HA and VA films are in the range of 27–42 nm and 8.36–8.39 Å, respectively (see Table II). We also note from Table II that the average grain size of HA films increases with RF power; on the other hand, grain refinement is seen in 200 W VA film due to the generation of impurity phases. Thus, the XRD data indicate that RF power plays an important role in determining the crystalline phases, grain sizes, and film textures.

To determine the effect of the presence of various iron oxides on the magnetic properties of *AG, HA, and VA films*, we measured in-plane *M–H* loops at 300 K, shown in Figure 2. The AG films show large non-saturation behaviors at higher magnetic fields (high-field susceptibility) and very small coercivity values within the experimental accuracy. The spontaneous magnetization ($4\pi M_S$) of AG films has a low value of 20 G in 50 W film, which rises for 100 W (370 G) and 200 W (1.2 kG), compared to the only 20% bulk Fe_3O_4 value of 5.9 kG. However, this 20% of bulk ($4\pi M_S$) value was improved significantly in HA and VA films (see Table II), while the former achieved 90% of the bulk value in 200 W film, and the latter has 71% of the bulk value in 100 W film. The low value of 34% in the 200 W VA film can be attributed to the presence of antiferromagnetic (FeO) and lesser magnetic (γ-Fe_2O_3) impurity phases. The increase in $4\pi M_S$ value in *HA* films as a function of RF power can be explained on the basis of grain growth (see supplementary Figure S1). However, the $4\pi M_S$ value still being lower than the bulk values can be attributed to the large grain boundary volume, which commonly observed in the nanocrystalline ferrite thin films.[18] Interestingly, HA and VA films show well-defined *M–H* loops with less high-field susceptibility values and reasonable coercivity (200−390 Oe) values compared to the AG films.

As a complementary technique to XRD, XPS study was carried out to support magnetic results to check whether there is a presence of any residual oxide phases other than Fe_3O_4 in our *HA* and *VA* samples. Fig. 3 shows the XPS signals of the Fe2p core level spectra consisting of two broad peaks of Fe-$2p_{1/2}$ at 710.22 eV and Fe-$2p_{3/2}$ at 724.04 eV, indicating presence of Fe_3O_4 phase.[17] The broadening of Fe-2p spectra is due to Fe_3O_4 contains mixed-valence Fe^{+3}

Table II Variation of $4\pi M_s$, lattice constant, and grain sizes in HA and VA films with RF power at 300 K.

HA films				VA films		
RF power (W)	$4\pi M_S$ (kG)	Lattice constant (Å)	Grain size (nm)	$4\pi M_S$ (kG)	Lattice constant (Å)	Grain size (nm)
50	4	8.36	27	3.1	8.38	21
100	4.8	8.38	33	4.2	8.38	24
200	5.3	8.39	42	2	8.40	20

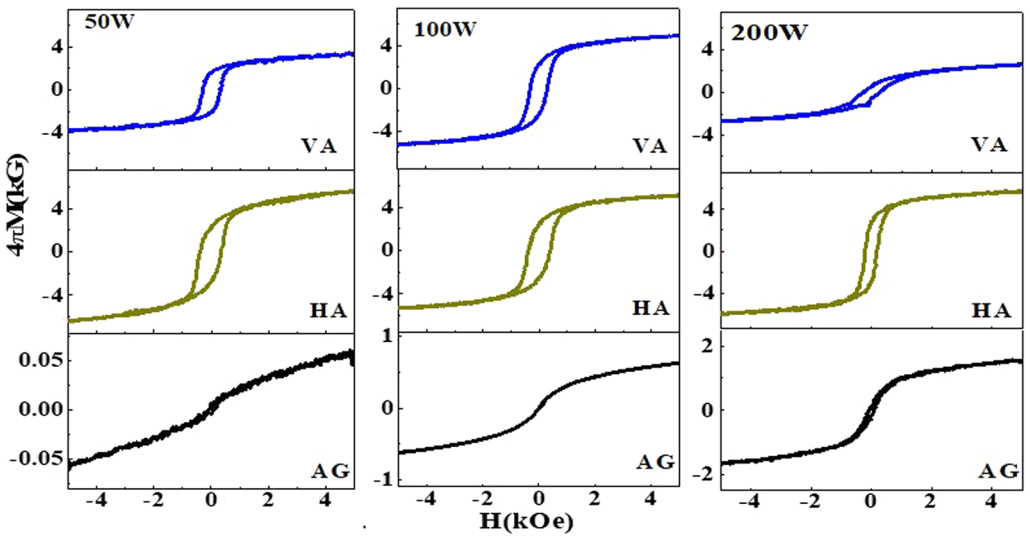

Fig. 2 M-H loops taken at 300 K for AG, HA, and VA films at different RF power.

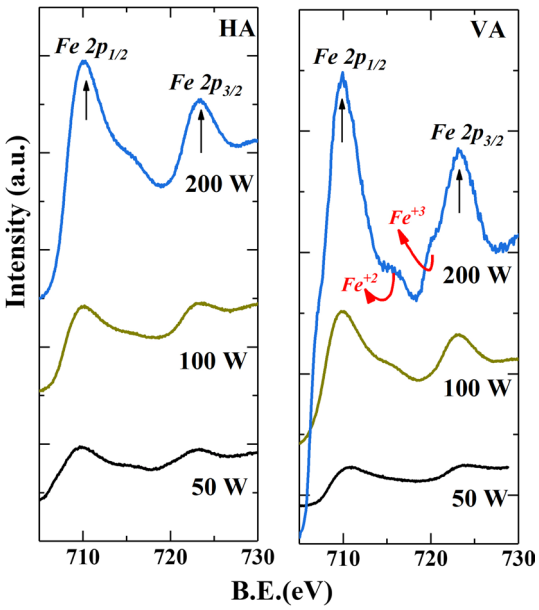

Fig. 3 Fe2p core-level XPS spectra of HA and VA films at different RF power.

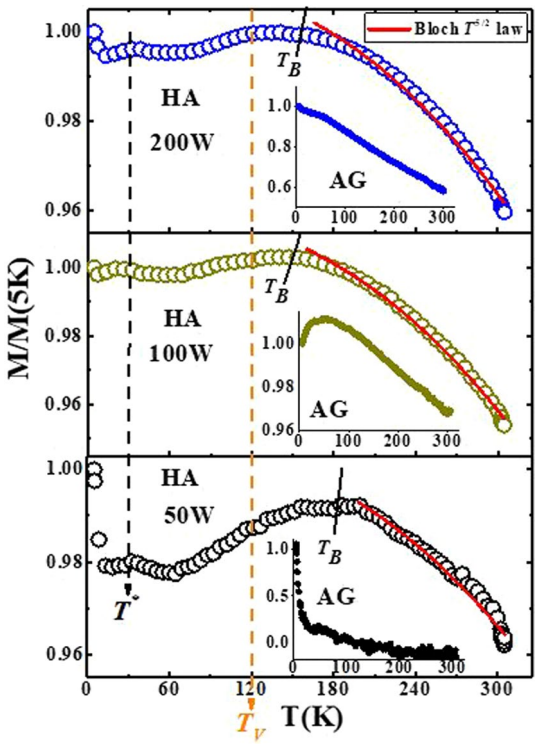

Fig. 4 M–T curves taken at 5 kOe for HA films at different RF power. The orange vertical dotted line represents Verwey transition temperature T_V. The T_B and T^* peaks indicate the blocking process of Fe_3O_4 grains and surface canted grains, respectively. Insets show corresponding M–T curves of AG films.

and Fe^{+2} ions in comparison to single Fe^{+3} ions in α-Fe_2O_3 and γ-Fe_2O_3 phases. However, two satellite peaks located around 714 eV and 719.8 eV can be seen in 200 W *VA* films, which are characteristic of Fe^{+3} and Fe^{+2} ions, respectively,[17] indicating the presence of residual FeO and γ-Fe_2O_3 phases that are not fully transformed into Fe_3O_4 phase.

From the above structural (XRD, XPS, and Raman spectra; see supplementary Figure S2) and magnetic studies, it is apparent that HA films are single-phase Fe_3O_4 with reasonably good $4\pi M_S$ values; therefore, we chose these films for further low-temperature magnetic and electric transport investigation. We plotted in Fig. 4 the normalized ZFC magnetization values, $M/M(5\text{ K})$, against increasing temperature from 5 K to 305 K at a fixed magnetic field of 5 kOe for HA films with respect to RF power. The magnetization of the HA films increases initially with decreasing temperature according to the Bloch law $M(T)=M_S(0)[1-(T/T_C)^n]$, with $n = 5/2$ instead of $n = 3/2$ (which is normally observed in ferromagnetic materials[17]). This deviation can be ascribed to the nanocrystalline nature of our HA films.[17] Notably, the ZFC magnetization behavior of HA films is dissimilar to the behavior of AG films (see insets), which show typical paramagnetic behavior in 50 W films and the mixture of paramagnetic and ferrimagnetic behaviors in 100 and 200 W films due to the presence of impurity iron oxide phases. Interestingly, HA films show broad maxima in ZFC magnetization curves (at different temperatures for different RF-power films) after which ZFC magnetization starts decreasing gradually. Typically, in interactive nanocrystalline ferromagnetic materials these broad maxima can be attributed to the blocking temperatures.[19,20] If this is the case, then smaller-grain-sized 50 W films should show lower blocking temperature (T_B) than the larger-grain-sized 100 and 200 W films, which is actually opposite the behavior observed in our study. This unusual ZFC magnetization behavior can be understood as follows: the drop in ZFC magnetization can be caused not only by the blocking temperature but also by the presence of the Verwey transition.[17] The Verwey transition normally occurs at temperature $T_V = 120$ K, wherein the structure of Fe_3O_4 changes from the high-temperature cubic to the low-temperature monoclinic phase, leading to the anisotropy change.[13] Therefore, in 100 and 200 W films, those with larger grain sizes and good $4\pi M_S$ should display Verwey transition and, because of overlapping of this with T_B, one would see a drop-in magnetization at a lower temperature. On the other hand, in the 50 W film, which has an inferior crystalline quality and low $4\pi M_S$ values, T_B may suppress the Verwey transition and we see the ZFC magnetization drop at higher temperatures. Further, at low temperatures around 30-50 K we see another shoulder-like peak (marked by T^*) in all HA films, which may correspond to the T_B of very small grain sizes or surface spin canting of nanograins, below which ZFC magnetization increases

rapidly again, as has been reported in laser-ablated Fe_3O_4 thin films.[17]

To understand the effect of various magnetic transitions in HA films, the ZFC *M*−*H* loops at 5 K and 300 K are plotted in low field regions (0−800 Oe) for comparative study, as shown in Fig. 5. Below either T_B or T_V, the coercivity (*Hc*) values are expected to increase because of spin blocking[19] in the former case and the high anisotropic monoclinic Fe_3O_4 phase[17] in the latter case. We observed almost twofold *Hc* enhancement in all HA films. Surprisingly, we can notice that 5 K *M*–*H* loops are asymmetric in 50 W films at origin with different *Hc*+ (750 Oe) and *Hc*−(640 Oe). This is a typical feature of exchange bias phenomena wherein interfacial interaction between antiferromagnetic (AFM) and ferromagnetic (FM) surfaces causes shifted *M*−*H* loops with increased coercivity when measured under FC conditions.[21] However, the observation of such exchange bias even for in the ZFC condition is interesting; this may be because of the surface canted spin of nanograins of HA films,[22] whose spins get blocked below T* < 50 K (see Fig. 4) and show AFM ordering which provides AFM/FM exchange interaction with ferrimagnetic Fe_3O_4 grains. However, this effect is less pronounced in higher-RF-power HA films compared to the 50 W films, as higher-RF-power films are better crystalline. This surface spin canting also results in larger non-saturation behaviors of *M*−*H* loops at high field (1000−5000 Oe) regions,[23] which is, otherwise in ferrimagnetic samples, expected to decrease at low temperatures. Hence, we can easily notice how various transitions affect the magnetic properties of nanocrystalline Fe_3O_4 films, which is otherwise difficult because the Verwey transition is extremely sensitive to the nanostructure sizes.[4]

Consistent with the ZFC magnetization study, the effect of nanocrystalline nature on the electric transport properties of HA films were examined by measuring resistivity (ρ) vs. temperature (T) curves shown in Fig. 6. The AG films of 50W and 100 W are highly insulating because of the presence of the α-Fe_2O_3 phase, which is beyond the measuring capability of our instrument but the room-temperature resistivity of 200 W film was measured as 0.96 Ω-cm. Room-temperature resistivity values of HA films are in the range of 40−450 mΩ-cm, however, which is higher than the single-crystal Fe_3O_4 resistivity value of 4 mΩ-cm.[13] This further confirms that annealing in wet H_2 transforms α-Fe_2O_3 into the Fe_3O_4 phase and improves the electric conductivity. The HA films do not show sharp Verwey transitions in resistivity data like the ZFC magnetization data, as normally observed in the single-crystal Fe_3O_4 at 120 K.[24] Although, the signature of some sort of charge ordering can be seen at different low-temperature regions. The suppression of sharp Verwey transitions in ρ vs. T curves compared to the M vs. T can be linked with defects, large grain boundary density, off stoichiometric Fe^{2+}/Fe^{3+} ratios, and micro/nano strains present in nanocrystalline Fe_3O_4 thin films, as has been explained in laser ablated Fe_3O_4 thin films.[25] The experimental ρ vs. T

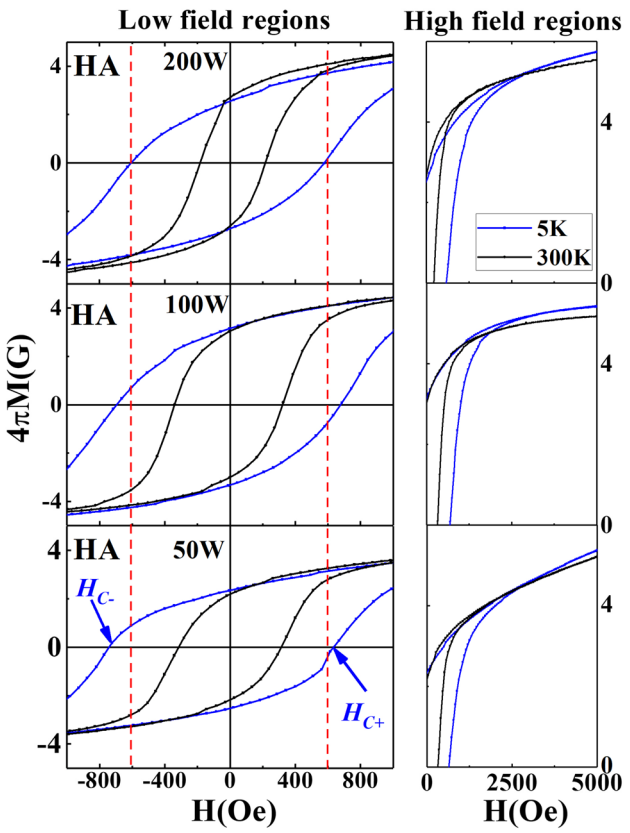

Fig. 5 ZFC M−H loops of HA films of different RF power taken at 5K and 300 K near origin and high field regions.

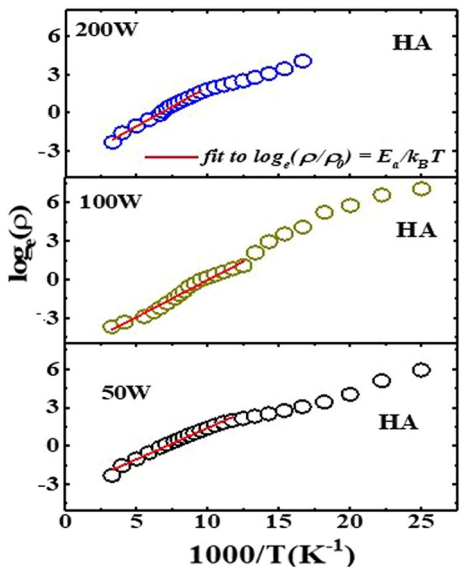

Fig. 6 $\log_e\rho$ vs. 1000/T curves for HA films at different RF power (open circle). Red solid lines represent $\log_e(\rho/\rho_0) = E_a/k_BT$ equation.

data of HA films could be linearized in the $log_e(\rho/\rho_0) - 1/T$ axis between 150 K and 300 K, suggesting a thermally activated hopping transport mechanism. The reasonably good fit gives the activation energy E_a of HA films in the range of (30−48) meV, which is comparable with the observed bulk value of 20–40 meV.[26]

Discussion

Based on different reduction conditions of VA and HA to obtain Fe_3O_4 thin films, we construct a phase diagram between temperature (T) vs. oxygen partial pressure $P(O_2)$ in Fig. 7. To understand crystalline phase formation in Fe_3O_4 thin films, phase diagrams of bulk formats are also included. The phase diagram for the bulk at thermal equilibrium follows successive reduction processes: $Fe_2O_3 \rightarrow \frac{2}{3} Fe_3O_4 + \frac{1}{6} O_2$, $Fe_3O_4 \rightarrow 3\,FeO + \frac{1}{2} O_2$ and $FeO \rightarrow Fe + \frac{1}{2} O_2$ at high T and low $P(O_2)$, as theoretically calculated (different solid color lines) by using Gibbs free energy $\Delta G^0 = -2.303\ RT\ log_e(P_{O2})$.[27,28] On the other hand, $Fe_2O_3 + \frac{1}{3} H_2 \rightarrow \frac{2}{3} Fe_3O_4 + \frac{1}{3} H_2O$ (dashed red line) process can be theoretically calculated by using Gibbs free energy $\Delta G^0 = -2.303\ RT\ log_e(P_{H2O}/P_{H2})$.[28,29] In this study, the major parameter is the annealing temperature, T and P_{O2} (VA films), and P_{H2O}/P_{H2} (HA films) because, irrespective of RF power, samples were annealed at the same conditions. The VA films (orange) and HA films (green) are represented by solid spheres in the phase diagram. Surprisingly, the transformation $Fe_2O_3 \rightarrow Fe_3O_4$ in VA films takes place at lower T and high $P(O_2)$ compared to the bulk equilibrium process, and in high RF films few impurity phases also appear, which is expected at extreme conditions (higher T and lower $P(O_2)$). Simultaneously, HA films exhibit the successful transformation of $Fe_2O_3 \rightarrow Fe_3O_4$ in all RF power samples. The progress of the partial transformation of $Fe_2O_3 \rightarrow Fe_3O_4$ with RF power in AG films is also approximated by the pink solid spheres positioned parallel to the temperature axis. These results indicate that the transformation of $Fe_2O_3 \rightarrow Fe_3O_4$ at the nanoscale is not the same as the bulk thermodynamic equilibrium process because of the increased surface-to-volume ratio and modified kinetics.

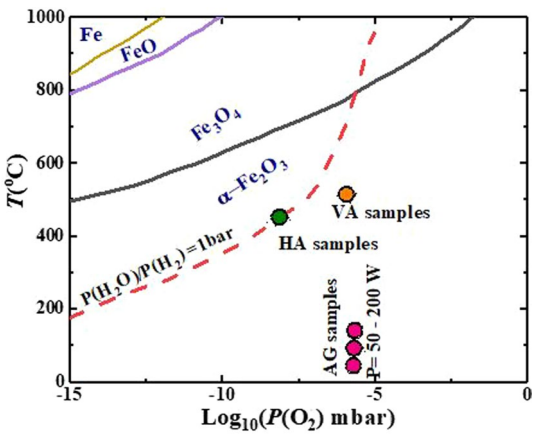

Fig. 7 Relation between $P(O_2)$ vs. T for thermal equilibrium between various Fe-O phases (solid lines) and dashed line shows H_2O isobar for 1 bar. Growth conditions of VA, HA, and AG films (color solid spheres).

It is interesting to note from this study that sputter power plays a significant role in determining the physical properties of Fe_3O_4 thin films even after the reduction process (VA and HA). For instance, (0) texture, smaller grain sizes, lower magnetization, and higher resistivity values are observed in low-sputter-power-grown Fe_3O_4 films compared to the randomly oriented high-sputter-power Fe_3O_4 films with improved magnetic and electric properties. Further, similar reduction conditions lead to different properties of films grown at different RF power. We believe that during the deposition of AG film, crystallites not detectable by XRD are formed, which act as nucleation centers for further crystallization during the VA and HA reduction processes. The sputtering process generally involves a complex series of collisions and energy transfers between many atoms; therefore, it is difficult to model the sputtering process effect based on various experimental parameters such as growth temperature, oxygen pressure, and RF power.[30] In the present case, the situation becomes more complicated since different reduction processes are involved. The structure of the Fe-based oxide is very sensitive to Fe/O ration and multiple ionic states of Fe. Due to a sharp phase boundary among the Fe_3O_4, Fe, FeO, and α-Fe_2O_3 phases,[7,27] the oxygen pressure condition has to be strictly satisfied.

Conclusions

We have examined different reduction processes of converting antiferromagnetic insulating α-Fe_2O_3 thin films into ferrimagnetic conducting Fe_3O_4 thin films. In particular, we investigated how the wet H_2 reduction process affects the formation of Fe_3O_4 nanocrystalline thin films, yielding contrasting magnetic properties compared with the bulk Fe_3O_4.

- While sputtering in an inert Ar atmosphere cannot produce single-phase Fe_3O_4 thin films from the α-Fe_2O_3 target at given RF power, wet H_2 annealing provides an efficient reduction process for the complete conversion when compared to vacuum annealing.
- It is also found that irrespective of the post-reduction process, sputtering RF power has left a signature in many physical properties such as grain sizes, texture, and corresponding magnetization values.
- Low-temperature magnetic studies on wet H_2 annealed films exhibit dramatic changes in the magnetic anisot-

ropy, Verwey transition, and canted magnetism in terms of broadening of maxima peaks T_B, reduction in the value of T_V, and exchange-shifted ZFC *M–H* loops.

- The larger resistivity compared to the bulk Fe_3O_4 and observation of faint Verwey transition can be ascribed to the nanograin sizes present in wet H_2 annealed films.
- Lastly, the observed phase diagram modulation in our Fe_3O_4 thin films compared to the bulk equilibrium, as presented, originates essentially from modified kinetics and thermodynamics of phase formation offered by nano-sized grains that possess a large surface-to-volume ratio.

Supplementary Information The online version contains supplementary material available at https://doi.org/10.1007/s11664-022-09566-y.

Acknowledgments The author thanks Dr. Prasad, Dr. Venkataramani and Dr. Sahoo from IIT-Bombay (India) for allowing the use of experimental facilities. The author also acknowledges the Ministry of Science and Technology (MOST), Taiwan, for financial support under Grants Nor. MOST-109-2112-M-110-012.

Conflict of interest The author declares that he has no known conflicting financial interests or personal relationships that could have appeared to influence the work reported in this paper.

References

1. A. Samrot, C.S. Sahithya, J.A. Selvarani, and P. Paulraj, *Curr. Res. Green Sustain. Chem.* 4, 100042 (2020).
2. M.S. Ansari, M.H.D. Othman, M.O. Ansari, S. Ansari, and H. Abdullah, *Appl. Mater. Today* 25, 101181 (2021).
3. G.S. Parkinson, *Surf. Sci. Rep.* 71, 1272 (2016).
4. J. Lee, S.G. Kwon, J.-G. Park, and T. Hyeon, *Nano Lett.* 15, 4337 (2015).
5. R. Sinmyo, E. Bykova, S.V. Ovsyannikov, C. McCammon, I. Kupenko, L. Ismailova, and L. Dubrovinsky, *Sci Rep* 6, 32852 (2016).
6. A. Namai, M. Yoshikiyo, K. Yamada, S. Sakurai, T. Goto, T. Yoshida, T. Miyazaki, M. Nakajima, T. Suemoto, H. Tokoro, and S.-I. Ohkoshi, *Nat Commun* 3, 1035 (2012).
7. S. Sakurai, A. Namai, K. Hashimoto, and S. Ohkoshi, *J. Am. Chem. Soc.* 131, 18299 (2009).
8. V. Ukleev, S. Suturin, T. Nakajima, T.-H. Arima, T. Saerbeck, T. Hanashima, A. Sitnikova, D. Kirilenko, N. Yakovlev, and N. Sokolov, *Sci Rep* 8, 8741 (2018).
9. H. Jani, J. Linghu, S. Hooda, R.V. Chopdekar, C. Li, G. Ji Omar, S. Prakash, Y. Du, P. Yang, A. Banas, K. Banas, S. Ghosh, S. Ojha, G.R. Umapathy, D. Kanjilal, A. Ariando, S.J. Pennycook, E. Arenholz, P.G. Radaelli, J.M.D. Coey, Y.P. Feng, and T. Venkatesan, *Nat Commun* 12, 1668 (2021).
10. S. Tong, C.A. Quinto, L. Zhang, P. Mohindra, and G. Bao, *ACS Nano* 11, 6808 (2017).
11. R. Ramos, T. Kikkawa, K. Uchida, H. Adachi, I. Lucas, M.H. Aguirre, P. Algarabel, L. Morellón, S. Maekawa, E. Saitoh, and M.R. Ibarra, *Appl. Phys. Lett.* 102, 072413 (2013).
12. P. Dey, R. Rawat, S.R. Potdar, R.J. Choudhary, and A. Banerjee, *J. Appl. Phys.* 115, 17C110 (2014).
13. M. Bohra, N. Agarwal, and V. Singh, *J. Nanomater.* 2019, 18 (2019).
14. P. Jimenez-Cavero, I. Lucas, A. Anadon, R. Ramos, T. Niizeki, M.H. Aguirre, P.A. Algarabel, K. Uchida, M.R. Ibarra, E. Saitoh, and L. Morellón, *APL Mater.* 5, 026103 (2017).
15. X.H. Liu, A.D. Rata, C.F. Chang, A.C. Komarek, and L.H. Tjeng, *Phys. Rev. B* 90, 125142 (2014).
16. S. Huang, S. Gu, K. Tang, J. Ye, Z. Xu, S. Zhu, and Y. Zheng, *J. Vac. Sci. Technol. B Nanotechnol. Microelectron: Mater, Process, Measurement, Phenom.* 32, 052801 (2014).
17. M. Bohra, K.E. Prasad, R. Bollina, S.C. Sahoo and N. Kumar, *J. Magn. Magn. Mater.* 418, 137 (2016).
18. J. Dash, S. Prasad, N. Venkataramani, P. Kishan, N. Kumar, S.D. Kulkarni, and S.K. Date, *J. Appl. Phys.* 86, 3303 (1999).
19. M. Bohra, V. Alman, A. Showry, V. Singh, R.E. Diaz, M. Sowwan, and P. Grammatikopoulos, *ACS Omega* 5, 32883 (2020).
20. M. Bohra, S. Prasad, N. Venkataramani, S.C. Sahoo, N. Kumar, and R. Krishnan, *IEEE Trans. Magn.* 49, 4249 (2013).
21. J. Nogués, and I.K. Schuller, *J. Magn. Magn. Mater.* 192, 203 (1999).
22. H. Roy Dakua, *AIP Advances* 10, 035324 (2020).
23. R.H. Kodama, A.E. Berkowitz, E.J. McNiff Jr., and S. Foner, *J. Appl. Phys.* 81, 5552 (1997).
24. X. Liu, C.-F. Chang, A.D. Rata, A.C. Komarek, and L.H. Tjeng, *npj Quant. Mater.* 1, 16027 (2016).
25. M. Bohra, D. Roy Chowdhury, J.-F. Bobo, and V. Singh, *J. Appl. Phys.,* 125, 013901 (2019).
26. K. Liu, L. Zhao, P. Klavins, F.E. Osterloh, and H. Hiramatsu, *J. Appl. Phys.* 93, 7951 (2003).
27. M.H. Hamed, D.N. Mueller, and M. Müller, *J. Mater. Chem. C* 8, 1335 (2020).
28. D. H. Wakelin, *The Making, Shaping and Treating of Steel*, 11th Edition – Ironmaking, 811 (1999).
29. G. Ketteler, W. Weiss, W. Ranke, and R. Schlögl, *Phys. Chem. Chem. Phys.* 3, 1114 (2001).
30. B.R. Acharya, S. Prasad, N. Venkataramani, S. Shringi, and R. Krishnan, *J. Appl. Phys.* 79, 478 (1996).